

# Spectrally accurate reverse-mode differentiable bounce-averaging operator and its applications

K. Unalmis<sup>1†</sup>, R. Gaur<sup>2</sup>, R. Conlin<sup>3</sup>, D. Panici<sup>2</sup>, and E. Kolemen<sup>2,4</sup>

<sup>1</sup>Electrical and Computer Engineering, Princeton University, NJ 08544, USA

<sup>2</sup>Mechanical and Aerospace Engineering, Princeton University, NJ 08544, USA

<sup>3</sup>IREAP, University of Maryland, College Park, MD 20740, USA

<sup>4</sup>Princeton Plasma Physics Laboratory, Princeton, NJ, USA

(Received xx; revised xx; accepted xx)

We present a spectrally accurate, automatically differentiable bounce-averaging operator implemented in the DESC stellarator optimization suite. Using this operator, we can perform efficient optimization of many objectives to improve stellarator performance, such as the  $\epsilon_{\text{eff}}^{3/2}$  proxy for the neoclassical transport coefficient in the  $1/\nu$  regime. By employing this differentiable approximation, for the first time, we directly optimize a finite- $\beta$  stellarator to reduce neoclassical transport using reverse-mode differentiation, ensuring that the computational cost of determining the gradients is independent of the number of input parameters.

## 1. Introduction

Stellarators, first conceived by [Spitzer Jr \(1958\)](#), represent a distinct approach to magnetic confinement fusion that offers unique advantages over tokamaks. These toroidal devices achieve plasma confinement through external magnetic fields rather than through plasma current, providing greater design flexibility and operational stability. The absence of a continuous toroidal symmetry allows for magnetic field optimization through boundary shaping, which helps minimize the net toroidal current and thereby avoid current-driven plasma instabilities and disruptions that plague tokamak operation ([Helander 2014](#)).

The design of optimal stellarator configurations is a complex optimization problem involving hundreds of degrees of freedom. Traditional optimization approaches have evolved significantly over the past decades. The VMEC (Variational Moments Equilibrium Code), developed by [Hirshman & Whitson \(1983\)](#), has served as the foundation for numerous stellarator optimization efforts. Building upon VMEC, several optimization frameworks have emerged: STELLOPT ([Lazerson \*et al.\* 2020](#); [Spong \*et al.\* 1998](#)), which implements a suite of physics-based optimization criteria; ROSE ([Drevlak \*et al.\* 2018](#)), which focuses on coil optimization and engineering constraints; and more recently, SIMSOPT ([Landreman \*et al.\* 2021](#)), which provides a flexible approach to stellarator optimization.

However, in general, traditional approaches rely on finite-difference techniques to compute gradients. Such techniques may not yield an accurate estimate of the gradient which can affect the optimizer convergence. Furthermore, the objective function must be recomputed to estimate the gradient for each optimizable parameter. In DESC, unlike previous optimizers, it is not necessary to resolve the MHD force balance equation at each optimization step. Additional objectives that depend on equilibrium force balance can be optimized simultaneously on a single device while ensuring ideal MHD force balance.

In this paper we present a fast, automatically-differentiable bounce-averaging operator

† Email address for correspondence: [kunalmis@princeton.edu](mailto:kunalmis@princeton.edu), [ekolemen@princeton.edu](mailto:ekolemen@princeton.edu)

which is used to simplify kinetic models such as drift and gyrokinetics. Specifically, we will focus on neoclassical transport in the  $1/\nu$  regime by evaluating and optimizing for the effective ripple (Nemov *et al.* 1999). The bounce-averaging operators and drift kinetic model is explained in the following sections. This operator is implemented as a part of the DESC (Dudt & Kolemen 2020; Panici *et al.* 2023; Conlin *et al.* 2023) optimization suite.

In section 2, we will briefly explain how we solve the ideal MHD equation and calculate an equilibrium using the DESC suite. In section 3, we will introduce the drift kinetic model and explain the derivation of neoclassical transport in the  $1/\nu$  collisionality regime, as done similarly by Nemov. In section 4, we explain our implementation of the reverse-mode differentiable proxy and demonstrate how it is faster than forward-mode computation. Section 5 describes the numerical methods for the optimization. In section 6, we present comparison of the effective ripple with the NEO code from the STELLOPT suite, and we optimize against neoclassical transport for various stellarator equilibria in section 7. In section 8, we conclude this work and explain how it can be extended.

## 2. Ideal MHD equilibrium

Our study only concerns solutions whose magnetic field lines lie on closed nested toroidal surfaces, known as flux surfaces. We label the flux surfaces with their enclosed toroidal flux  $\psi$ . On each flux surface, curves of constant  $\alpha$  correspond to magnetic field lines. A divergence-free magnetic field can be written in the Clebsch form (D’haeseleer *et al.* 2012).

$$\mathbf{B} = \nabla\psi \times \nabla\alpha. \quad (2.1)$$

In a set of specialized coordinates, known as flux coordinates,  $\alpha = \theta_P - \iota\phi$  where  $\theta_P$  is a PEST poloidal angle,  $\phi$  is the toroidal angle of the cylindrical coordinate system  $(R, \phi, Z)$ , and the quantity

$$\iota = \frac{\mathbf{B} \cdot \nabla\theta_P}{\mathbf{B} \cdot \nabla\phi}, \quad (2.2)$$

is the pitch of the field line on a flux surface, commonly referred to as the rotational transform. The definition of  $\mathbf{B}$  in (2.1) is consistent with (2.2). We solve the steady-state, ideal MHD (MagnetoHydroDynamic) equation

$$\nabla \left( \mu_0 p + \frac{|B|^2}{2} \right) = \mathbf{B} \cdot \nabla \mathbf{B} \quad (2.3)$$

which describes a balance between the plasma pressure  $p$ , magnetic field pressure  $|B|^2$  and the effect of field line curvature  $\mathbf{B} \cdot \nabla \mathbf{B}$ . Unlike a tokamak, we cannot simplify (2.3) to a two-dimensional scalar Grad-Shafranov equation. Assuming the existence of nested flux surfaces, we can only reduce (2.3) to two coupled three-dimensional equations.

The maps in the MHD equation are derived from Fourier-Zernike series. These orthogonal polynomials enable efficient computation of derivatives and ensures smoothness of the solution, in particular regularity near the magnetic axis (Dudt & Kolemen 2020; Panici *et al.* 2023). This boundary value problem is then solved as a minimization problem using a trust-region method. Since DESC is written in JAX, the computation is typically accelerated on a GPU. In the following section, we explain the drift-kinetic model.

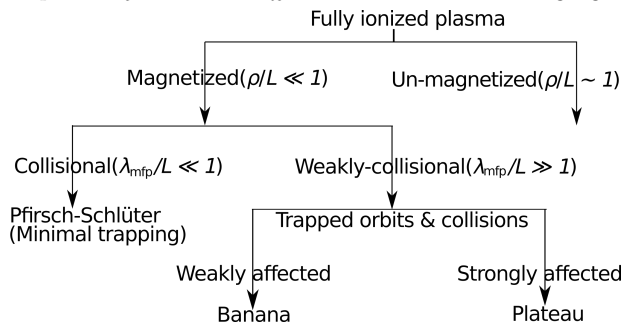


Figure 1: Schematic categorizing neoclassical transport. Most fusion stellarator designs lie in the banana regime where the effective ripple quantifies transport best.

### 3. Neoclassical model of plasma

The dynamics of a magnetized hot plasma differ significantly from that of an unmagnetized fluid. Unlike isotropic hard-sphere collisions that govern the behavior of an uncharged fluid, a plasma behaves differently in directions perpendicular and parallel to the magnetic field lines because of Coulomb collisions. In magnetized plasmas, particles traverse helical trajectories around magnetic field lines, exhibiting motion characterized by gyration around these lines and drifts across them. The classical transport model assumes a simplistic view of particle collisions and does not adequately incorporate the effects of these drifts. To correctly account for the effect of drifts, trapped and passing particles, and the magnetic geometry, we use the neoclassical transport theory.

There are three fundamental length and time scales relevant to magnetized plasmas. The time scales correspond to the particle transit frequency  $v_{\text{th},s}/L$ , where  $v_{\text{th},s} = \sqrt{2T_s/m_s}$  is the thermal speed, the Coulomb collision frequency  $\nu_{ss'} \propto T^{3/2}$ , and the gyration (cyclotron) frequency  $\Omega_s = Z_s e |B| / (m_s c)$  where  $s, s'$  are the species of interest. For each time scale, the corresponding length scales are the gradient scale length of the magnetic field  $L$ , the mean free path  $\lambda_{\text{mfp}}$ , and the gyroradius  $\rho_s = v_{\text{th},s} / \Omega_s$ , respectively. In a magnetized plasma,

$$\nu_{ss'} \sim \frac{v_{\text{th},s}}{L} \ll \Omega_s \quad \lambda_{\text{mfp}} \sim L \gg \rho_s \quad (3.1)$$

Using a random walk estimate, we can calculate the classical heat transport coefficient in the perpendicular direction as  $D_{\perp} \sim \nu_{ss'} \rho_s^2 \sim T^{5/2}$  (Helander & Sigmar 2005) whereas, using neoclassical theory, we have  $\Delta x \sim \rho_s |B| / |B_p|$ ,  $|B|$  and  $|B_p|$  are the total and poloidal magnetic field strength, respectively which gives  $D_{\perp} \sim \nu_{ss'} \rho_s^2 |B|^2 / |B_p|^2 \sim T^{5/2} |B|^2 / |B_p|^2$ . The ratio  $|B| / |B_p|$  strongly depends on the magnetic field geometry and significantly affects the regime of neoclassical transport.

A magnetized plasma can either be weakly or strongly collisional. This is defined by the collisionality  $\nu_* \equiv L / \lambda_{\text{mfp}} = \nu / (v_{\text{th},s} / L)$ . In a strongly collisional plasma, particles undergo frequent collisions without covering a significant distance along a magnetic field line, *i.e.*,  $\nu_* \gg 1$ . Conversely, in a weakly collisional plasma, particles can traverse and move along the field line multiple times before colliding, *i.e.*,  $\nu_* \ll 1$ . Stellarator plasmas in practical applications tend to be weakly collisional.

Based on the stellarator geometry, the weak collisionality regime can be further divided into the banana or plateau regime depending on the inverse aspect ratio  $\epsilon \sim q |B_p| / |B|$ . Most stellarators lie in the banana regime, where the collisionality  $\nu_* \ll \epsilon^{3/2}$ . Therefore, we want to minimize neoclassical transport in the banana regime. This categorization is illustrated in figure 1.

For the banana regime, Nemov *et al.* (1999) first derived a simplified form of the effective ripple proxy by systematically simplifying the neoclassical equation. This process is explained in the following section.

### 3.1. Effective ripple

In this section, we explain in detail the derivation of the effective field ripple similar to the one used by Nemov *et al.* (1999). For a particle with mass  $m$ , let  $v_{\parallel}$  and  $v_{\perp}$  be the velocity parallel and perpendicular, respectively, to the unit vector magnetic field  $\mathbf{b}$ . In the limit of low collisionality  $\nu^* \ll \epsilon^{3/2}$ , the neoclassical model studies the distribution of plasma determined by solving the drift-kinetic equation.

$$\mathbf{v}_{Ds} \cdot \nabla F_0 + |v_{\parallel}| \mathbf{b} \cdot \nabla F_1 = \mathcal{C}[F_1] \quad (3.2)$$

The background Maxwellian distribution function is parameterized by  $F_0: \psi, \alpha, \zeta, E$  and the higher-order correction to the Maxwellian by  $F_1: \psi, \alpha, \zeta, E, \mu$ . In this partial differential equation, the velocity space has two independent coordinates: the total kinetic energy  $E$  and the magnetic moment  $\mu = m|v_{\perp}|^2/(2|B|)$ .<sup>†</sup> The Clebsch coordinates  $(\psi, \alpha, \zeta)$  may be chosen to specify the position. The gradient  $\nabla$  is a spatial derivative. Likewise, the partial derivatives with respect to  $\mu$  or  $E$  are taken at fixed position. With these conventions, the Lorentz or pitch-angle scattering collision operator is written

$$\mathcal{C}[F_1] = m\nu|v_{\parallel}| \frac{\partial}{\partial \mu} \mu \frac{|v_{\parallel}|}{|B|} \frac{\partial F_1}{\partial \mu} \quad (3.3)$$

where the collision frequency  $\nu$  depends only on the energy of the particle. Often, the Lorentz operator is written as a function of the pitch angle  $\lambda = \mu/E$ . The effect of the electric field was ignored as our study focuses on the low collisionality regime. Also recall

$$\mathbf{v}_{Ds} = \frac{1}{\Omega_s} \left[ |v_{\parallel}|^2 \mathbf{b} \times (\mathbf{b} \cdot \nabla \mathbf{b}) + \frac{|v_{\perp}|^2}{2|B|} \mathbf{b} \times \nabla |B| \right] \quad (3.4)$$

Now to further simplify the drift-kinetic equation, we average the bounce motion of the particles for a particle with constant pitch angle

$$\bar{X} = \left( \oint |v_{\parallel}|^{-1} d\ell \right)^{-1} \oint X |v_{\parallel}|^{-1} d\ell \quad (3.5)$$

where  $\ell$  is the length along the field line. Using the streamline property of a magnetic field in these curvilinear coordinates,

$$\frac{d\ell}{|B|} = \frac{d\zeta}{\mathbf{B} \cdot \nabla \zeta} \quad (3.6)$$

the bounce averaging operator can be written as follows.

$$\bar{X} = \left( \oint |v_{\parallel}|^{-1} \frac{d\zeta}{\mathbf{b} \cdot \nabla \zeta} \right)^{-1} \oint X |v_{\parallel}|^{-1} \frac{d\zeta}{\mathbf{b} \cdot \nabla \zeta} \quad (3.7)$$

Section 5.1 discusses this operator in more detail. Bounce averaging the drift-kinetic equation (3.2) yields

$$\overline{\mathbf{v}_{Ds} \cdot \nabla \alpha \frac{\partial F_0}{\partial \alpha}} + \overline{\mathbf{v}_{Ds} \cdot \nabla \psi \frac{\partial F_0}{\partial \psi}} = m\nu \frac{\partial}{\partial \mu} \mu I \frac{\partial F_1}{\partial \mu} \quad (3.8)$$

where  $I = \overline{|v_{\parallel}|/|B|}$ . Assume that the binormal component of the magnetic drift is much

<sup>†</sup> The gyrophase angle specifying the third coordinate can be ignored in this treatment.

smaller than the radial component  $\overline{\mathbf{v}_{Ds} \cdot \nabla \alpha} \ll \overline{\mathbf{v}_{Ds} \cdot \nabla \psi}$  to simplify the bounce-averaged neoclassical equation.

$$\overline{\mathbf{v}_{Ds} \cdot \nabla \psi} \frac{\partial F_0}{\partial \psi} = m\nu \frac{\partial}{\partial \mu} \mu I \frac{\partial F_1}{\partial \mu} \quad (3.9)$$

To invert the collision operator, we use the following identity and the ideal MHD force balance equation (2.3). First label the geodesic curvature of the field line  $\kappa_G = [\mathbf{b} \times (\mathbf{b} \cdot \nabla \mathbf{b})] \cdot \nabla \psi$ . Then

$$\mathbf{v}_{Ds} \cdot \nabla \psi = -\frac{|v_{\parallel}|}{3} \frac{\partial}{\partial \mu} (3v^2 |v_{\parallel}| + |v_{\parallel}|^3) \frac{\kappa_G}{\Omega_s} \quad (3.10)$$

$$\begin{aligned} \overline{\mathbf{v}_{Ds} \cdot \nabla \psi} &= -\frac{1}{3} \left( \oint \frac{d\zeta}{\mathbf{b} \cdot \nabla \zeta} |v_{\parallel}|^{-1} \right)^{-1} \oint \frac{d\zeta}{\mathbf{b} \cdot \nabla \zeta} \frac{\partial}{\partial \mu} (3v^2 |v_{\parallel}| + |v_{\parallel}|^3) \frac{\kappa_G}{\Omega_s} \\ &= -\frac{1}{3} \frac{\partial}{\partial \mu} H \end{aligned} \quad (3.11)$$

Now the bounce-averaged neoclassical equation (3.9) is integrated in  $\mu$ .

$$-\frac{1}{3} \frac{\partial}{\partial \mu} \left[ H \frac{\partial F_0}{\partial \psi} \right] = \frac{\partial}{\partial \mu} \left[ m\nu \mu I \frac{\partial F_1}{\partial \mu} \right] \quad (3.12)$$

$$\frac{\partial F_1}{\partial \mu} = -\frac{\partial F_0}{\partial \psi} \frac{H}{3m\nu \mu I} \quad (3.13)$$

In stellarator optimization a goal is to minimize the radial particle flux. For a tractable optimization, the flux surface average of this quantity is of interest to minimize. This is an average over a differential volume that encloses the flux surface.

$$\Gamma = \int dS |\nabla \psi|^{-1} \int d^3 \mathbf{v} F_1 \overline{\mathbf{v}_{Ds} \cdot \nabla \psi} \quad (3.14)$$

$$= \int dS |\nabla \psi|^{-1} \int d^3 \mathbf{v} \frac{-|v_{\parallel}|}{3} \frac{\partial}{\partial \mu} (3v^2 |v_{\parallel}| + |v_{\parallel}|^3) \frac{\kappa_G}{\Omega_s} F_1 \quad (3.15)$$

To calculate the velocity integral, we shall use two different coordinate representations of the velocity space:  $(E, \mu)$  and  $(E, \varrho)$  where  $B_0 \varrho = E/\mu = 1/\lambda$  is the inverse pitch angle, and  $B_0$  is a background magnetic field. In these coordinates

$$\frac{1}{2\pi} \int d^3 \mathbf{v} = |B| \int_0^\infty dE \int_0^{E/|B|} \frac{d\mu}{|v_{\parallel}|} \quad (3.16)$$

$$= \frac{|B|}{B_0} \left( \frac{m}{2} \right)^{1/2} \sum_\sigma \int_0^\infty dE E^{1/2} \int_\infty^{\min|B|/B_0} \frac{d\varrho}{\varrho^2 (1 - |B|/(B_0 \varrho))^{1/2}} \quad (3.17)$$

Using the velocity integral in  $(E, \mu)$ , applying integration by parts in the  $\mu$  coordinate, and enforcing the boundary condition  $\lim_{|v_{\parallel}| \rightarrow \infty} F_1 = 0$ , we can rewrite the particle flux

$$\Gamma = \left( \int \frac{d\zeta}{\mathbf{b} \cdot \nabla \zeta} |\nabla \psi| \right)^{-1} \int d^3 \mathbf{v} \frac{\partial F_1}{\partial \mu} H \quad (3.18)$$

Finally, denoting the average major radius of the stellarator by  $R_0$ , writing  $\partial F_0 / \partial \psi = (\partial F_0 / \partial r) / \langle |\nabla \psi| \rangle$  in (3.13) where  $r$  is a dimensionless radial coordinate, and using the velocity integral in pitch angle coordinates  $(E, \varrho)$ , the flux surface-averaged radial particle

flux (3.15) can be written as an integration along field lines over all ripple wells.

$$\Gamma(\psi) = \epsilon_{\text{eff}}^{3/2} \int \frac{\partial F_0}{\partial r} E^{3/2} dE \quad (3.19)$$

$$\epsilon_{\text{eff}}^{3/2}(\psi) = \frac{R_0^2}{16\sqrt{2}\langle|\nabla\psi|\rangle^2} \int_0^{2\pi} M(\psi, \alpha) d\alpha \quad (3.20)$$

$$\langle|\nabla\psi|\rangle = \left( \int |\nabla\psi|^{-1} dS \right)^{-1} \int dS \quad (3.21)$$

$$M(\psi, \alpha) = \lim_{\zeta_2 - \zeta_1 \rightarrow \infty} \left( \int_{\zeta_1}^{\zeta_2} \frac{d\zeta}{\mathbf{B} \cdot \nabla\zeta} \right)^{-1} \int_{\varrho_{\min}}^{\varrho_{\max}} d\varrho \sum_w \frac{\hat{H}^2}{\hat{I}}(\psi, \alpha, \varrho, w) \quad (3.22)$$

$$\hat{H}(\psi, \alpha, \varrho, w) = \int_{\zeta_1(w)}^{\zeta_2(w)} \left( 1 - \frac{|B|}{B_0\varrho} \right)^{1/2} \left( 4 \frac{B_0\varrho}{|B|} - 1 \right) |\nabla\psi|_{\kappa_G} \frac{d\zeta}{\mathbf{B} \cdot \nabla\zeta} \varrho^{-3/2} \quad (3.23)$$

$$\hat{I}(\psi, \alpha, \varrho, w) = \int_{\zeta_1(w)}^{\zeta_2(w)} \left( 1 - \frac{|B|}{B_0\varrho} \right)^{1/2} \frac{d\zeta}{\mathbf{B} \cdot \nabla\zeta} \quad (3.24)$$

The number  $w$  indexes the ripple well with boundaries  $\zeta_1(w)$  and  $\zeta_2(w)$  where a bouncing particle is trapped. In an axisymmetric device, field line integration over a single poloidal transit is sufficient to capture a surface integral. For a non-axisymmetric configuration, convergence occurs in the limit of an infinite number of transits for an irrational magnetic surface. For a rational or near-rational surface, it is necessary to average over multiple field lines until the surface is covered sufficiently.

Since  $\epsilon_{\text{eff}}^{3/2}$  is a purely geometry-dependent term, reducing it by varying the stellarator plasma boundary can reduce the radial neoclassical loss of the trapped particles. To ensure low neoclassical transport and high performance, we typically optimize a stellarator such that  $\epsilon_{\text{eff}} \sim 10^{-2}$ .

#### 4. Reverse-mode differentiable bounce-averaging

Optimizing to reduce the effective ripple involves four tasks.

- (i) Computing physical quantities using configuration parameters  $\mathbf{p}_i$ . For the magnetic field, we use the notation  $\mathbf{B} = \mathbf{B}(\mathbf{p}_i)$ .
- (ii) Root finding for bounce points  $\zeta_{k,w}(\psi, \alpha, \lambda)$  such that  $\lambda|B|(\psi, \alpha, \zeta_{k,w}) = 1$ .
- (iii) Integration throughout the plasma volume and velocity space.
- (iv) Computing objective gradients and performing a particular [optimization](#).

Section 5 further explains the algorithm. Briefly, since bounce averaging is defined on a flux surface, the physical quantities are approximated with Fourier series. The mapping from the curvilinear flux coordinates  $(\psi, \theta, \zeta)$  that admit more spectrally condensed Fourier transforms to the Clebsch field line coordinates  $(\psi, \alpha, \zeta)$  is approximated with Fourier-Chebyshev series on each surface. The velocity space grid is discretized with  $N_\varrho$  uniformly spaced inverse pitch angle values  $B_0\varrho \in (\min|B|, \max|B|)$ . A global root-finding algorithm with resolution labeled by  $Y_B$  computes the bounce points over  $N_l$  toroidal transits. High-order quadrature with resolution  $N_q$  estimate the bounce averages. Section 5.4 further explains the quadrature technique.

In a forward mode operation, the derivative is

$$\frac{\partial \epsilon_{\text{eff}}^{3/2}}{\partial \mathbf{p}_i} = \frac{\partial \mathbf{B}}{\partial \mathbf{p}_i} \frac{\partial \zeta_{k,w}}{\partial \mathbf{B}} \frac{\partial \epsilon_{\text{eff}}}{\partial \zeta_{k,w}} \frac{\partial \epsilon_{\text{eff}}^{3/2}}{\partial \epsilon_{\text{eff}}} \quad (4.1)$$

For each parameter, `jax` defines the sequence of operations and calculates the partial derivatives. This chain rule must be performed separately for each parameter and scales linearly with the number of parameters  $N_p$ . In a realistic stellarator optimization  $N_p \sim 10^3$ . On the other hand, for a reverse-mode operation, we first do a single forward pass to store the structure of operators and all intermediate operations without calculating derivatives and then sequentially compute gradients.

$$\frac{\partial \epsilon_{\text{eff}}^{3/2}}{\partial \epsilon_{\text{eff}}} = \frac{3}{2} \epsilon_{\text{eff}}^{1/2} \rightarrow \frac{\partial \epsilon_{\text{eff}}^{3/2}}{\partial \zeta_{k,w}} = \frac{\partial \epsilon_{\text{eff}}^{3/2}}{\partial \epsilon_{\text{eff}}} \frac{\partial \epsilon_{\text{eff}}}{\partial \zeta_{k,w}} \rightarrow \frac{\partial \epsilon_{\text{eff}}^{3/2}}{\partial \mathbf{B}} = \frac{\partial \epsilon_{\text{eff}}^{3/2}}{\partial \zeta_{k,w}} \frac{\partial \zeta_{k,w}}{\partial \mathbf{B}} \rightarrow \frac{\partial \epsilon_{\text{eff}}^{3/2}}{\partial \mathbf{p}_i} = \frac{\partial \epsilon_{\text{eff}}^{3/2}}{\partial \mathbf{B}} \frac{\partial \mathbf{B}}{\partial \mathbf{p}_i} \quad (4.2)$$

Thus by utilizing the inverse approach, the problem size of the differentiation relies only on the output variable's dimension, which, in the case of surface-averaged quantities such as  $\epsilon_{\text{eff}}$ , is the number of flux surfaces over which the computation is performed. Nevertheless, a lengthy sequence of intermediate operations can cause memory to become a limiting factor. Checkpointing schemes and the construction of custom adjoints for groups of intermediate operations are two strategies that are typically used to minimize the memory cost of reverse-mode differentiation (Sapienza *et al.* 2024).

## 5. Methods

The implementation is written in Python using Google's JAX library (Bradbury *et al.* 2018) and is simultaneously compatible with the scientific computing packages `jax.numpy` and `numpy`, taking advantage of the simpler maintainability of Python code, while ensuring that computational operations are performed efficiently. JIT (Just-In-Time) compilation in JAX is used to compile Python code into machine code at runtime to recover performance similar to that of low-level programming languages.

### 5.1. Bounce integral

The bounce-averaged drift between the bounce points  $\zeta_1(w)$  and  $\zeta_2(w)$  of magnetic well  $w$  where the parallel velocity of the particle vanishes  $|v_{\parallel}|(\zeta_{k,w}) = 0$  for  $i \in \{1, 2\}$  is given by

$$\overline{v_{\text{drift}}} = (t(\zeta_2) - t(\zeta_1))^{-1} \int_{t(\zeta_1)}^{t(\zeta_2)} v_{\text{drift}} dt \quad (5.1)$$

Since the dynamics parallel to the field lines dominate, the particle trajectory is approximated to follow field lines by parameterizing time as the distance along a field-line following coordinate  $dt = d\ell/|v_{\parallel}|$ . By conservation of the first adiabatic invariant and conservation of energy, the pitch angle  $\lambda = \mu/E$  of a bouncing particle stays nearly constant over the timescale to complete bounce orbits. Using the streamline property in curvilinear coordinates (3.6) and  $|v_{\parallel}| = \sqrt{2E/m} \sqrt{1 - \lambda|B|}$ ,

$$\overline{v_{\text{drift}}} = \left( \int_{\zeta_1}^{\zeta_2} (1 - \lambda|B|)^{-1/2} \frac{|B|}{\mathbf{B} \cdot \nabla \zeta} d\zeta \right)^{-1} \int_{\zeta_1}^{\zeta_2} v_{\text{drift}} (1 - \lambda|B|)^{-1/2} \frac{|B|}{\mathbf{B} \cdot \nabla \zeta} d\zeta \quad (5.2)$$

where the bounce points  $\zeta_{k,w}$  depend on the particle's pitch such that  $\lambda|B|(\zeta_{k,w}) = 1$ .

A desirable feature of this formulation is that specialized quadrature (section 5.4) can estimate drifts with spectral accuracy, whereas an approach that instead iterates the original differential equation describing the particle dynamics may have difficulty resolving short wavelength modes which arise from the singular features near the bounce points.

Many stellarator optimization proxies require computation of a set of such integrals

throughout the plasma volume.

$$\mathcal{F} = \{F(\psi, \alpha, \lambda, w) \mid 1/\lambda \in (\min|B|, \max|B|)\} \quad (5.3)$$

$$F(\psi, \alpha, \lambda, w) = \int_{\zeta_1(w)}^{\zeta_2(w)} f(\psi, \alpha, \lambda, \zeta, \{G_i(\psi, \alpha, \zeta)\}) d\zeta \quad (5.4)$$

where  $f$  denotes some composition operator on a set of smooth functions  $\{G_i\}$ . Often  $|(\partial f/\partial \zeta)_{\psi, \alpha, \lambda}| \rightarrow \infty$  as  $\zeta$  approaches the integration boundary. The set of integrals  $\mathcal{F}$  is infinite in general. The accurate estimation of these many locally defined singular integrals makes evaluation of such proxies more expensive than typical.

### 5.1.1. Cost

For a computation on  $N_s$  flux surfaces, where the field line traced on each flux surface has  $N_w$  magnetic wells for each of  $N_p$  pitch angles, there will be  $(N_s N_w N_p)$  bounce integrals to compute. With  $N_q$  quadrature points for each integration, the integrand is evaluated at  $N_s N_w N_p N_q \sim 10^8$  points. The parametrization of  $f$  using  $(\psi, \alpha, \zeta)$  coordinates is generally unknown *a priori* because the equilibrium perturbations during optimization move the field line, thereby altering the path of integration. With an additional  $N_i$  Newton iterations to solve for the coordinate mapping  $\theta(\psi, \alpha, \zeta)$  to evaluate  $f$  under a known parametrization,  $f(\psi, \theta, \zeta, \lambda)$ , the computation cost becomes  $\mathcal{O}(N_c N_i N_s N_w N_p N_q)$  where  $N_c$  is the number of spectral coefficients used to approximate  $f$ . Furthermore, automatic differentiation of the objective with respect to the optimizable parameters incurs an expense that is linear in the problem size. These costs make it necessary to develop an efficient algorithm.

## 5.2. Function approximation

DESC solves the inverse equilibrium problem. The computational domain is parameterized by the curvilinear toroidal coordinates  $(\rho, \theta, \zeta) \in [0, 1] \times \mathbb{R} \times \mathbb{R}$  where  $\rho$  is a function of the toroidal flux  $\psi$  and  $\theta, \zeta$  are arbitrary angles. These coordinates are related to the Clebsch coordinates  $(\psi, \alpha, \zeta)$  defined through the maps

$$\alpha: \rho, \theta, \zeta \mapsto \theta_P(\rho, \theta, \zeta) - \iota(\rho)\phi(\rho, \theta, \zeta) \quad (5.5)$$

$$\theta_P: \rho, \theta, \zeta \mapsto \theta + \Lambda(\rho, \theta, \zeta) \quad (5.6)$$

$$\phi: \rho, \theta, \zeta \mapsto \zeta + \omega(\rho, \theta, \zeta) \quad (5.7)$$

where  $\Lambda, \omega$  are poloidal, toroidal stream functions, respectively, and  $\iota$  is the rotational transform defined in (2.2). The stream functions relate the angles  $\theta, \zeta$  that are used to parameterize the plasma boundary  $R(\theta, \zeta), Z(\theta, \zeta)$  with those that make the magnetic field lines straight in the  $(\theta_P, \phi)$  plane. Fourier-Zernike series expansions, with coefficients determined by the optimizer, approximate the stream functions  $\Lambda$  and  $\omega$ .

The optimization proxies that involve bounce averaging are typically functions of distance along field lines between bounce points, and this requires that the surface average be performed by integration along curves of constant  $\rho$  and  $\alpha$ . Computing the values  $\theta$  along a field line denoted by  $(\rho_i, \alpha_i)$  requires solving a nonlinear relation pointwise for the  $\theta^*$  values which satisfy

$$\alpha(\rho_i, \theta^*, \zeta) = \alpha_i \quad (5.8)$$

The solution to this relation is unique, and it is best found with Newton iteration. To avoid repeating this expensive root-finding problem at each quadrature point, the inverse map of (5.5) is estimated. Recall that the frequency transform of the map  $\rho, \alpha, \zeta \mapsto \theta(\rho, \alpha, \zeta)$  under the chosen basis must be concentrated at low frequencies for the series to converge



fast. For periodic (non-periodic) maps, the standard choice for the basis is a Fourier (Chebyshev) series [Boyd \(2013\)](#). Both converge exponentially for smooth maps, but the larger region of convergence in the complex plane of Fourier series makes it preferable to construct coordinate systems such that the function to approximate is periodic. One reason Chebyshev polynomials are preferred to other orthogonal polynomials or prolate spheroidal wave functions is fast discrete polynomial transforms are less efficient than discrete cosine transforms. Equation (5.8) is solved on a fixed tensor-product grid in  $(\rho, \alpha, \zeta) \in [0, 1] \times [0, 2\pi]^2$  on the Fourier nodes in  $\alpha$  and Chebyshev nodes in  $\zeta$ . These values  $\theta(\rho, \alpha, \zeta)$  on each flux surface are interpolated to a Fourier-Chebyshev series by the real FFT and DCT.

$$\theta: \rho, \alpha, \zeta \mapsto \sum_{mn} t_{mn}(\rho) \exp(im\alpha) T_n(\zeta) \quad (5.9)$$

Partial summation techniques are used to increase evaluation speed. When the optimizer perturbs the spectral coefficients of the stream functions, the root-finding in (5.8) are initialized with the previous solution.

It should be noted that (5.9) estimates the inverse map of (5.5) over a single branch cut of  $\alpha$ . That is, the expansion for  $\theta$  above will differ depending on the value of  $k \in \mathbb{Z}$  that determines the domain for  $\alpha \in [2\pi k, 2\pi(k+1))$ . This follows from the definition of  $\alpha$  in  $\mathbf{B} = \nabla\psi \times \nabla\alpha$  on an irrational magnetic surface which implies the angle  $\theta(\rho, \alpha, \zeta)$  is multivalued at a physical location. In particular, following an irrational field, the single-valued  $\theta \in \mathbb{R}$  grows unbounded as  $|\zeta| \rightarrow \infty$ . Therefore, it is impossible to approximate the map  $\rho, \alpha, \zeta \mapsto \theta(\rho, \alpha, \zeta)$  using single-valued basis functions defined on a compact set as such an approximation attains a finite maximum. Likewise,  $\alpha$  is multivalued. As the field line is followed, the label may jump to  $\alpha \notin [2\pi k, 2\pi(k+1))$  after completing some toroidal transit. Hence,  $\theta(\rho, \alpha, \zeta)$  must be periodic in  $\alpha$  with period  $2\pi$ . At every point  $\zeta_p \in [2\pi k, 2\pi\ell]$  where  $k, \ell \in \mathbb{Z}$  where the field line completes a poloidal transit there is guaranteed to exist a discrete jump discontinuity in the approximation for  $\theta$  at  $\zeta = 2\pi\ell(p)$ , starting the toroidal transit. Still, it suffices to interpolate  $\theta$  over one branch cut. To recover the single-valued  $\theta$  from the Fourier-Chebyshev interpolation over one branch cut, at  $\zeta = 2\pi k$  for every  $k \in \mathbb{Z}$  we can add an integer multiple of  $2\pi$  to the next cut of  $\theta$ .<sup>†</sup>

### 5.3. Off-grid interpolation

The Zernike polynomials are orthogonal basis functions on the unit disc. The 2D coupling of this basis is designed to concentrate the frequency transform of maps on the unit disc at lower frequencies than geometry-agnostic tensor-product basis such as Fourier-Chebyshev. Boyd shows the required number of spectral coefficients is typically half that of Fourier-Chebyshev ([Boyd & Yu 2011](#)). Hence an optimization that varies a finite number of coefficients in the Fourier-Zernike series expansions for  $R, Z, A, \omega$  at a time will have more freedom compared to expansions under other basis. However, fast transforms and their approximate non-uniform generalizations, cannot interpolate this basis as they can the Fourier-Chebyshev basis.

Because the magnetic field lines vary throughout an optimization, optimization of these objectives necessarily involves “off-grid” interpolation ([Boyd 2013](#), section 10.7).

<sup>†</sup> A necessary condition for recovering the true  $\theta$  from its interpolation over one branch cut is for the approximation to not enforce  $\theta(\rho, \alpha, \zeta) = \theta(\rho, \alpha, \zeta + 2\pi k)$  for  $k \in \mathbb{Z}$ . For this reason, the map  $\rho, \alpha, \zeta \mapsto \theta(\rho, \theta_P(\rho, \alpha, \zeta), \zeta)$  is not interpolated with Fourier series in  $\theta_P, \zeta$  because it is impossible to approximate an unbounded function with a finite Fourier series. Due to Gibbs effects, this statement holds even when the goal is to approximate  $\theta$  over one branch cut. The proof uses analytic continuation.

Here the locally defined and singular nature of the bounce integrals demands that the evaluation grid be non-uniform while the optimization objective requires this grid to be time-dependent. Such interpolation where the basis functions cannot be precomputed dominates the cost of pseudo-spectral algorithms.

To mitigate these effects we reduce the dimensionality of the series expansions. The implemented algorithm computes the Fourier-Zernike basis functions prior to the optimization on a fixed tensor-product grid in  $(\rho, \theta, \zeta)$  with uniformly spaced nodes in  $(\theta, \zeta) \in [0, 2\pi) \times [0, 2\pi/\text{NFP})$  where the field period NFP denotes the discrete integer periodicity of the boundary in  $(\theta, \zeta) \in [0, 2\pi)^2$  coordinates. The smooth periodic maps  $\{G_i\}$  in the integrands of the bounce integrals are computed on this grid through evaluation of  $R, Z, A, \omega$ . These values are interpolated to a Fourier series in  $(\theta, \zeta) \in [0, 2\pi) \times [0, 2\pi/\text{NFP})$  by the real fast Fourier transform. This approach minimizes the cost by reducing the number of spectral coefficients, replacing Zernike polynomials with the complex exponential basis functions which are cheaper to evaluate, and bypassing the operations to later compute  $\{G_i\}$  from  $R, Z, A, \omega$  at the quadrature nodes. The maps  $\{G_i\}$  are evaluated at the quadrature points from these Fourier series using non-uniform fast transforms, enabling evaluation with linearithmic cost in the number of spectral coefficients and points.

$$G: \rho, \alpha, \zeta \mapsto \sum_{mn} g_{mn}(\rho) \exp(i[m\theta(\rho, \alpha, \zeta) + n\zeta]) \quad (5.10)$$

#### 5.4. Quadrature

To compute the bounce points, we find the solutions  $\zeta_{k,w}(\rho, \alpha, \lambda)$  to  $\lambda|B|(\rho, \alpha, \zeta_{k,w}) = 1$  using global root-finding algorithms. The points  $\zeta_{k,w}$  are refined with the Newton method. The periodic smooth components of the integrand are interpolated to the quadrature points with non-uniform FFTs. High-order quadratures estimate (5.4) after resolving the singularity. Bounce integrals with bounce points where the derivative of  $|B|$  does not vanish have  $1/2$  power law singularities. However, strongly singular integrals where the domain of the integral ends at the local extrema of  $|B|$  are not integrable. Hence, everywhere except for the extrema, the quadrature discussed below captures the integral. The set of pitch angles which yield diverging integrals has measure zero, so we neglect their contribution when integrating over the velocity space.

Gaussian quadrature methods approximate the integral

$$\int_{-1}^1 \varsigma(x)f(x) dx \approx \sum_i \sigma_i f(x_i) \quad (5.11)$$

for some weight function  $\varsigma$  positive and continuous on  $(-1, 1)$ , by replacing  $f$  with its Hermite interpolation polynomial and choosing  $\sigma_i, x_i$  to not require evaluation of the derivative. To estimate singular integrals, a change of variable whose Jacobian decays to zero slowly near the singularity can transform the integrand into a well-behaved function that can be approximated by a polynomial. It is important that the transformation accounts exactly for the order of the singularity to prevent unnecessary clustering of quadrature points. For bounce integrals, we define  $\mathbb{D} = [-1, 1]$

$$a_1: \begin{cases} \mathbb{D} \rightarrow [\zeta_1, \zeta_2] \\ x \mapsto (x+1)(\zeta_2 - \zeta_1)/2 + \zeta_1 \end{cases} \quad (5.12)$$

$$a_2: \begin{cases} \mathbb{D} \rightarrow \mathbb{D} \\ x \mapsto \sin(\pi x/2) \end{cases} \quad (5.13)$$

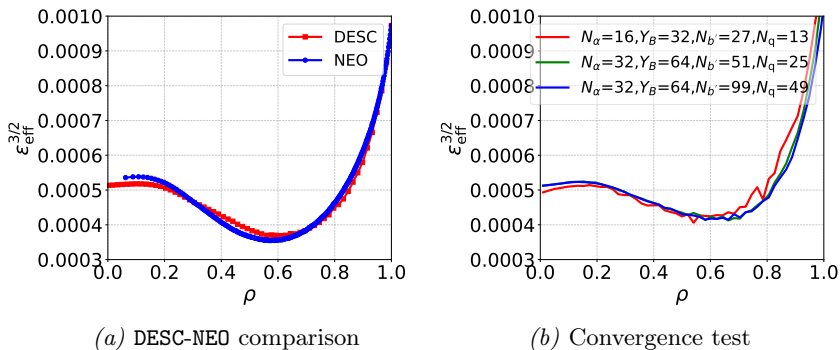


Figure 2: Figure (a) shows the neoclassical transport coefficient computed by DESC and NEO for the standard W7-X configuration. Figure (b) shows a resolution scan of the  $\epsilon_{\text{eff}}^{3/2}$ . There is reasonable agreement with a minor difference at the magnetic axis  $\rho = 0$  and  $\rho = 0.5$ .

and define  $x$  such that  $a_1(a_2[x]) = \zeta$ , so that the integral in (5.4) becomes

$$F = \int_{\zeta_1}^{\zeta_2} f(\zeta) d\zeta = \int_{-1}^1 f(a_1(a_2[x])) \frac{da_1}{da_2} \frac{da_2}{dx} dx \quad (5.14)$$

For bounce integrals with weakly singular  $f$  the resulting integrand is smooth and periodic, so a midpoint scheme in the variable  $x$  is used. This is identical to the second kind Chebyshev quadrature in the variable  $a_1^{-1}(\zeta)$  on  $f(a_1^{-1}(\zeta))/\sqrt{1 - (a_1^{-1}(\zeta))^2}$ . For bounce integrals with strongly singular  $f$  the resulting integrand is smooth, so Gauss-Legendre quadrature in the variable  $x$  is used. Appendix A illustrates the convergence.

## 6. Comparison with NEO

In this section, we will benchmark the bounce-averaging operator by comparing the neoclassical transport metric  $\epsilon_{\text{eff}}^{3/2}$  computation between the DESC and the neoclassical transport code NEO. For this, we choose the standard W7-X equilibrium given in the `desc/examples` directory in the DESC repository (Dudt *et al.* 2024). Comparison plots are provided in figure 2.

For this comparison, the spectral resolution used by DESC for the map (5.9) between flux coordinates that parameterize the boundary and field line coordinates is  $N_\alpha = 32$ ,  $N_\zeta = 64$ . The surface average is approximated with  $N_w = 640$  wells over 32 toroidal transits. The quadrature resolutions are  $N_\varrho = 100$ ,  $N_q = 50$ . The minor disagreement is likely because the approach used in this work is higher-order accurate. Moreover, unlike the NEO code, a Boozer transform to a coordinate system which broadens the frequency spectrum of maps is not required.

## 7. Optimizing stellarators for reduced neoclassical transport

Here we show an optimization in DESC starting from a finite- $\beta$  helically omnigenous (OH) equilibrium. The parameter  $\beta = 2\mu_0 p/|B|^2$  is the ratio of the plasma pressure to the magnetic pressure. We target flux surfaces near the boundary to reduce the effective ripple while maintaining reasonable elongation and curvature. The objective function

$$\mathcal{F} = A f_{\text{aspect}}^2 + C f_{\text{curv}}^2 + E f_{\text{elongation}}^2 + R f_{\text{ripple}}^2 \quad (7.1)$$

contains multiple quadratic penalty terms. The finite- $\beta$  OH equilibrium along with the definitions of the curvature and elongation objectives are provided in [Gaur \*et al.\* \(2024\)](#) ([Gaur 2024](#)). Using DESC, we then perform optimization and minimize  $\mathcal{F}$  while ensuring ideal MHD force balance [2.3](#) in the existing equilibrium.

$$\min \mathcal{F}(\mathbf{p}) \quad \text{s.t.} \quad \nabla \left( \mu_0 p + \frac{|B|^2}{2} \right) - \mathbf{B} \cdot \nabla \mathbf{B} = 0 \quad (7.2)$$

where  $\mathbf{p}$  represents a set of parameters that determine the pressure, rotational transform profiles, and boundary shape coefficients. An optimization takes less than two hours on an NVIDIA A100 GPU ([NVIDIA Corporation 2020](#)). The initial and optimized results are presented in [figure 3](#). More examples and tutorials for optimization are provided in the [documentation](#).

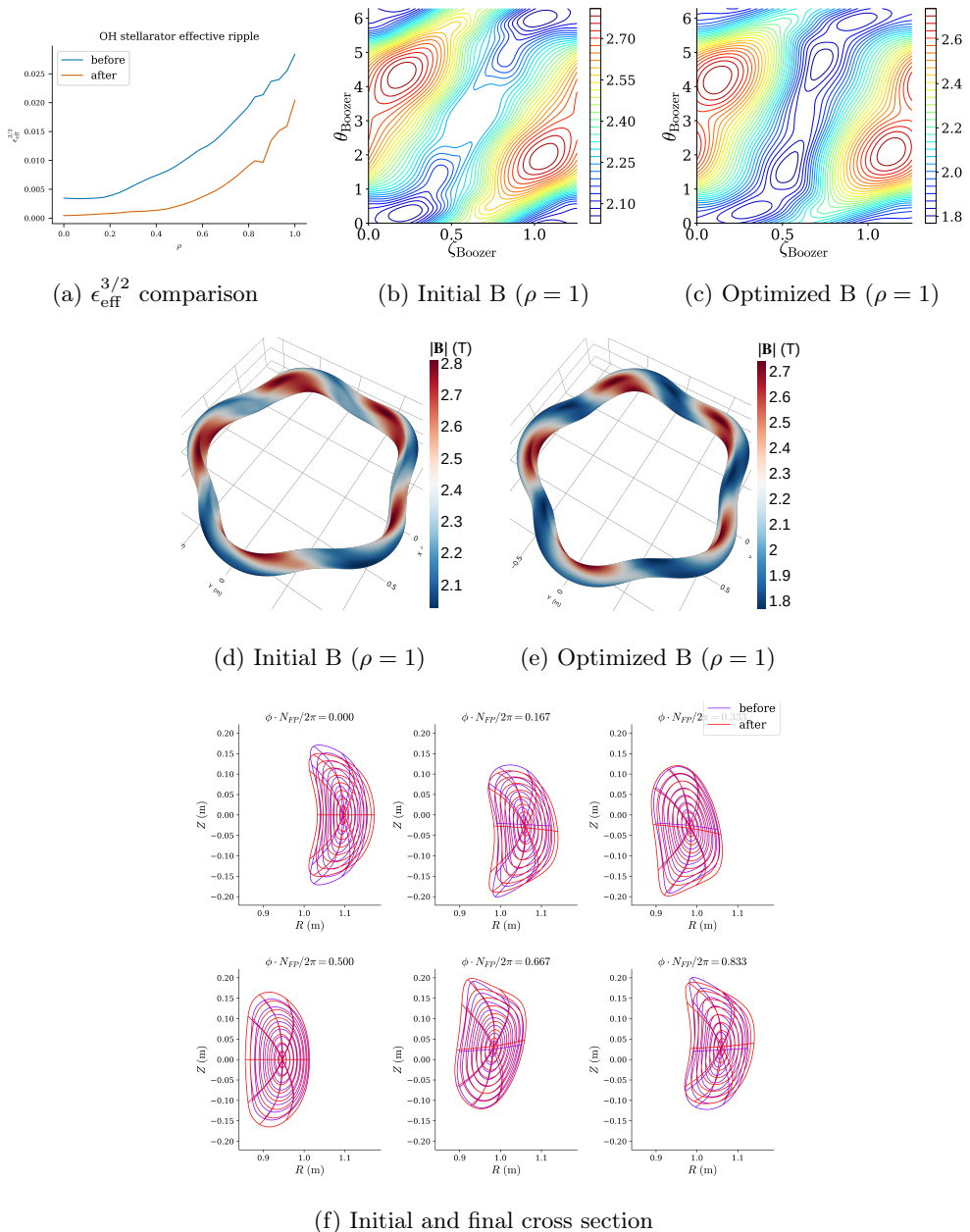


Figure 3: Outputs from the OH transport optimization in DESC. Figures (a) shows comparison of  $\epsilon_{\text{eff}}^{3/2}$  and figures (b), (c) show the magnetic field strength  $|B|$  on the boundary surface, in Boozer coordinates, respectively; (d), (e) illustrate the magnetic field strength on the plasma boundary, and (f) compares the initial and optimized boundary cross-section at different toroidal angles for a single field period.

## 8. Summary and Conclusions

In this work, we implemented a spectrally accurate, reverse-mode differentiable, bounce-averaging operator in the DESC (Dudt *et al.* 2025) stellarator optimization suite. We derived and benchmarked the neoclassical transport proxy  $\epsilon_{\text{eff}}$ . We explained how reverse-mode calculation is faster than forward-mode gradient calculation. Finally, we optimized a finite- $\beta$  configuration for reduced neoclassical transport using reverse-mode differentiation in DESC.

Many objectives of interest for stellarator performance rely on bounce-averaging. These include maximization of the second adiabatic invariant  $J_{\parallel} = \oint |v_{\parallel}| d\ell$ , proxies for gyrokinetic turbulence such as the available energy (Mackebach *et al.* 2022), objectives for trapped-electron mode turbulence, and proxies for energetic particle transport (Velasco *et al.* 2021). Using the bounce averaging operator we have added objectives for energetic particle transport (Nemov *et al.* 2008) to the DESC stellarator code. Some of these objectives have had limited use in optimization loops due to expensive computation requirements or difficulty finding desirable configurations in the optimization landscape. Future work (Hibbard *et al.* 2024) would involve demonstrating optimization for energetic particle confinement.

### Acknowledgements

This work is funded through the SciDAC program by the US Department of Energy, Office of Fusion Energy Science, and Office of Advanced Scientific Computing Research under contract No. DE-AC02-09CH11466, DE-SC0022005, Field Work Proposal No. 1019, and the Peter B. Lewis Fund for Student Innovation in Energy and the Environment. This research used the computing resources of the Della cluster at Princeton University.

## Appendix A. Quadrature convergence

We compare the following quadratures in their ability to compute elliptic integrals, which is similar to the bounce integrals in a simple stellarator geometry, as well as two more cases, realistic and degenerate, that model particles trapped in “W”-shaped wells.

- (i) Uniform trapezoidal
- (ii) Simpson’s 3/8
- (iii)  $\tanh - \sinh$  double exponential (DE)
- (iv) Gauss-Chebyshev of the first (GC<sub>1</sub>) and second kind (GC<sub>2</sub>)
- (v) Gauss-Legendre (GL) with a  $\sin$  transformation

$$F\left(\sin^{-1}(k), \frac{1}{k}\right) / k \equiv \int_0^{\sin^{-1}(k)} \frac{1}{\sqrt{k^2 - \sin(\zeta)^2}} d\zeta = K(k) \quad (\text{A } 1)$$

$$kE\left(\sin^{-1}(k), \frac{1}{k}\right) \equiv \int_0^{\sin^{-1}(k)} \sqrt{k^2 - \sin(\zeta)^2} d\zeta = E(k) + (k^2 - 1)K(k) \quad (\text{A } 2)$$

The last equality in (A 1) comes from (B 15) and (A 2) comes from (B 16). To understand the performance of the quadratures in a more realistic magnetic field for stellarators, we construct two “W”-shaped wells in Figures 6 and 7 and compute  $\int_{-1}^1 f(\zeta) d\zeta$  where  $f(\zeta)$  is  $1/\sqrt{2 - |B|(\zeta)}$  or  $\sqrt{2 - |B|(\zeta)}$ , corresponding to a strong and weak singularity, respectively.

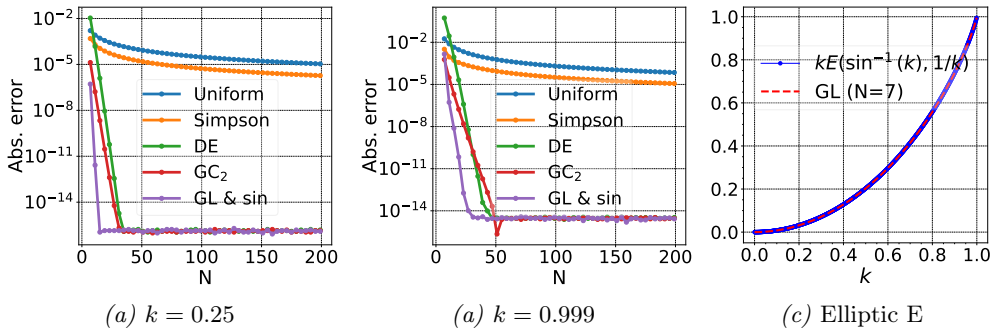


Figure 4: Convergence of various quadrature methods used to calculate the incomplete elliptic integral of the second kind. Gauss-Chebyshev, Gauss-Legendre, and double exponential quadrature show exponential convergence.

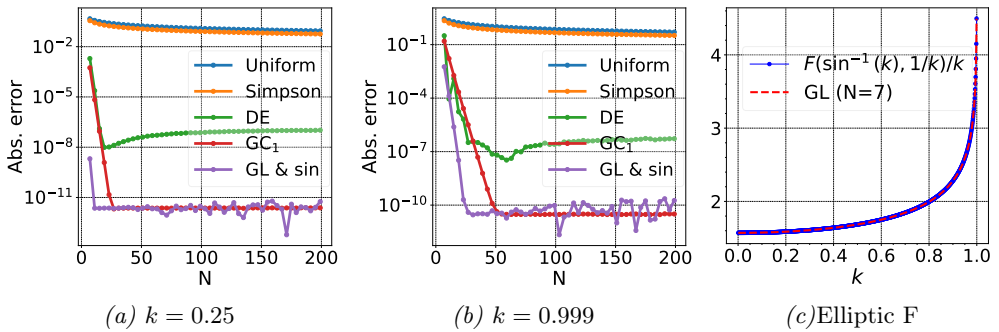
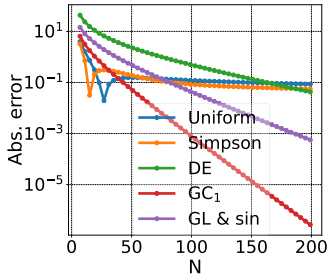
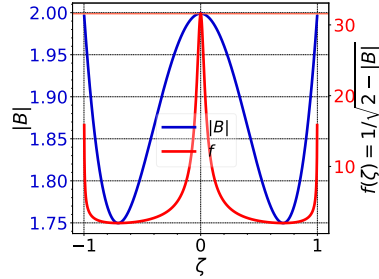


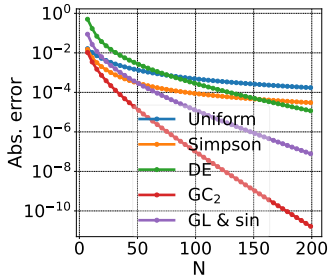
Figure 5: Convergence of various quadrature methods used to calculate the incomplete elliptic integral of the first kind. Gauss-Chebyshev, Gauss-Legendre quadratures show exponential convergence whereas Uniform, Simpson, and double exponential quadratures hit floating point plateaus early.



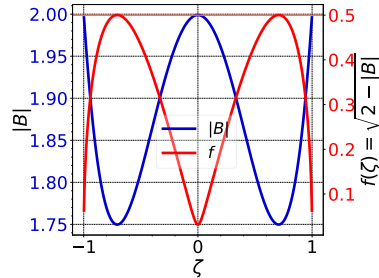
(a) Convergence plots



(b) Deep well, strong singularity

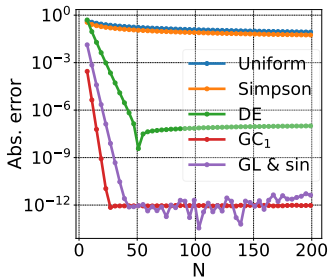


(c) Convergence plots

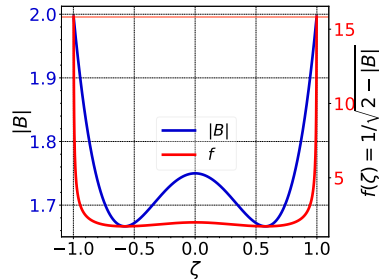


(d) Deep well, weak singularity

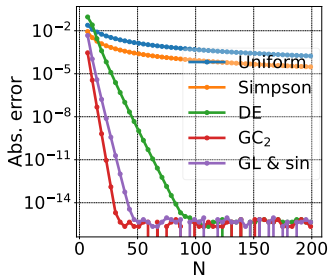
Figure 6: Quadrature comparison for deep “W”-shaped wells.



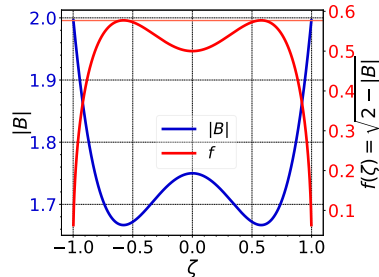
(a) Convergence plots



(b) Shallow well, strong singularity



(c) Convergence plots



(d) Shallow well, weak singularity

Figure 7: Quadrature comparison for shallow “W”-shaped wells.



## Appendix B. Bounce-averaged drifts in shifted-circle model

In a shifted-circle model for plasma equilibrium, we can approximately solve for analytic expressions for bounce averaged drifts. In this model, the magnetic field can be written

$$\mathbf{B} = \nabla\alpha \times \nabla\chi = F\nabla\phi + \frac{d\chi}{dr} \frac{r}{R_0} \nabla\theta_P \quad (\text{B } 1)$$

where the field line label  $\alpha = \phi - (1/\iota)\theta_P$ ,  $F$  is the enclosed poloidal current,  $\chi$  is poloidal flux, and  $\theta_P$  is a field line following coordinate. For this model, to lowest order, the Grad-Shafranov equation can be solved to obtain the constant solution  $F = F_0$  and to the next order  $dp/d\rho = -(F_0/R^2)dF/d\rho$  where  $\rho = r/a_N$  where  $a_N$  is the minor radius of the boundary. To first order, the poloidal field can be ignored and the magnetic field strength can be written as  $|B| = B_0(1 - \varepsilon \cos \theta_P)$ , where  $\varepsilon = r/R_0 \ll 1$  is the inverse aspect ratio. The geometric coefficients are defined below.

$$\text{gradpar} = \mathbf{b} \cdot \nabla\theta_P = G_0(1 - \varepsilon \cos \theta_P) \quad (\text{B } 2)$$

The integrated local shear labeled by gds21, with  $\hat{s}$  defining the global shear, is

$$\hat{s} = -\frac{\rho}{\iota} \frac{d\iota}{d\rho} \quad (\text{B } 3)$$

$$\alpha_{\text{MHD}} = -\frac{0.5}{\iota^2} \frac{dP}{d\rho} \quad (\text{B } 4)$$

$$\text{gds21} = \frac{d\chi}{d\rho} \frac{d(1/\iota)}{d\rho} \nabla\chi \cdot \nabla\alpha = -\hat{s} \left( \hat{s}\theta_P - \frac{\alpha_{\text{MHD}}}{|B|^4} \sin \theta_P \right) + \mathcal{O}(\varepsilon) \quad (\text{B } 5)$$

and the binormal component of the  $\nabla|B|$  drift

$$(\nabla|B|)_{\text{drift}} = \frac{1}{|B|^3} (\mathbf{B} \times \nabla|B|) \cdot \nabla\alpha \quad (\text{B } 6)$$

$$\begin{aligned} &= f_2 \left[ -\hat{s} + \left( \cos \theta_P - \frac{\text{gds21}}{\hat{s}} \sin \theta_P \right) \right] \\ &= f_2 \left[ -\hat{s} + \left( \cos \theta_P + \hat{s}\theta_P \sin \theta_P - \frac{\alpha_{\text{MHD}}}{B_0^4} \sin(\theta_P)^2 \right) \right] + \mathcal{O}(\varepsilon) \end{aligned} \quad (\text{B } 7)$$

where we have used (B5) to obtain the final expression for  $(\nabla|B|)_{\text{drift}}$  and all the expressions are normalized. The geometric factor corresponding to the binormal component of the curvature drift is

$$\text{cvdrift} = \frac{1}{|B|^3} [\mathbf{B} \times \nabla(p + |B|^2/2)] \cdot \nabla\alpha \quad (\text{B } 8)$$

$$= (\nabla|B|)_{\text{drift}} + f_3 \frac{1}{|B|^3} \frac{dP}{d\rho} \quad (\text{B } 9)$$

$$= f_2 \left[ -\hat{s} + \left( \cos \theta_P + \hat{s}\theta_P \sin \theta_P - \frac{\alpha_{\text{MHD}}}{B_0^4} \sin(\theta_P)^2 \right) \right] + f_3 \frac{\alpha_{\text{MHD}}}{B_0^2} + \mathcal{O}(\varepsilon) \quad (\text{B } 10)$$

The quantities  $f_2$  and  $f_3$  are scalar factors which contain a number of constants. The bounce-averaged drift is

$$\overline{v_D} = \left( \int_{\theta_{P,b1}}^{\theta_{P,b2}} \frac{d\theta_P}{\mathbf{b} \cdot \nabla\theta_P} |v_{\parallel}|^{-1} \right)^{-1} \int_{\theta_{P,b1}}^{\theta_{P,b2}} \frac{d\theta_P}{\mathbf{b} \cdot \nabla\theta_P} \left[ |v_{\parallel}| \text{cvdrift} + \frac{|v_{\perp}|^2}{2|v_{\parallel}|} (\nabla|B|)_{\text{drift}} \right] \quad (\text{B } 11)$$

where  $\theta_{P,b1}$  and  $\theta_{P,b2}$  are bounce angles. As used in Connor *et al.* and shown by Hegna, in the limit of a large aspect ratio shifted circle model, the parallel speed of a particle

with a fixed energy is

$$|v_{\parallel}| = \sqrt{2E/m} \sqrt{1 - \lambda|B|} = \sqrt{2E/m} \sqrt{2\varepsilon\lambda B_0} \sqrt{k^2 - \sin(\theta_P/2)^2} \quad (\text{B } 12)$$

where the parameter

$$k^2 = \frac{1}{2} \left( \frac{1 - \lambda B_0}{\varepsilon\lambda B_0} + 1 \right) \quad (\text{B } 13)$$

is a reparametrization of the pitch angle. Using these geometric simplifications, and  $|v_{\perp}|^2/2 = E - |v_{\parallel}|^2/2$ ,

$$\begin{aligned} \overline{v_D} = & \left( \int_{-2\sin^{-1}(k)}^{2\sin^{-1}(k)} \frac{d\theta_P}{\mathbf{b} \cdot \nabla\theta_P} \frac{1}{\sqrt{2\varepsilon\lambda B_0}} \frac{1}{\sqrt{k^2 - (\sin(\theta_P/2))^2}} \right)^{-1} \\ & \int_{-2\sin^{-1}(k)}^{2\sin^{-1}(k)} \frac{d\theta_P}{\mathbf{b} \cdot \nabla\theta_P} \left[ \sqrt{2\varepsilon\lambda B_0} \sqrt{k^2 - (\sin(\theta_P/2))^2} \text{cvdrift} \right. \\ & \quad \left. - \frac{\sqrt{2\varepsilon\lambda B_0} \sqrt{k^2 - (\sin(\theta_P/2))^2}}{2} (\nabla|B|)_{\text{drift}} \right. \\ & \quad \left. + \frac{1}{\sqrt{2\varepsilon\lambda B_0}} \frac{1}{\sqrt{k^2 - (\sin(\theta_P/2))^2}} \frac{(\nabla|B|)_{\text{drift}}}{2} \right] \quad (\text{B } 14) \end{aligned}$$

The following identities simplify (B 14). The incomplete elliptic integrals are converted to complete elliptic integrals using the Reciprocal-Modulus transformation (first two relations below) (Olver *et al.* 2024).

$$l_0 = \int_{-2\sin^{-1}(k)}^{2\sin^{-1}(k)} \frac{d\theta_P}{\sqrt{k^2 - \sin(\theta_P/2)^2}} = 4K(k) \quad (\text{B } 15)$$

$$l_1 = \int_{-2\sin^{-1}(k)}^{2\sin^{-1}(k)} d\theta_P \sqrt{k^2 - \sin(\theta_P/2)^2} = 4 [E(k) + (k^2 - 1)K(k)] \quad (\text{B } 16)$$

$$l_2 = \int_{-2\sin^{-1}(k)}^{2\sin^{-1}(k)} \frac{d\theta_P}{\sqrt{k^2 - \sin(\theta_P/2)^2}} \theta_P \sin(\theta_P) = 16 [E(k) + (k^2 - 1)K(k)] \quad (\text{B } 17)$$

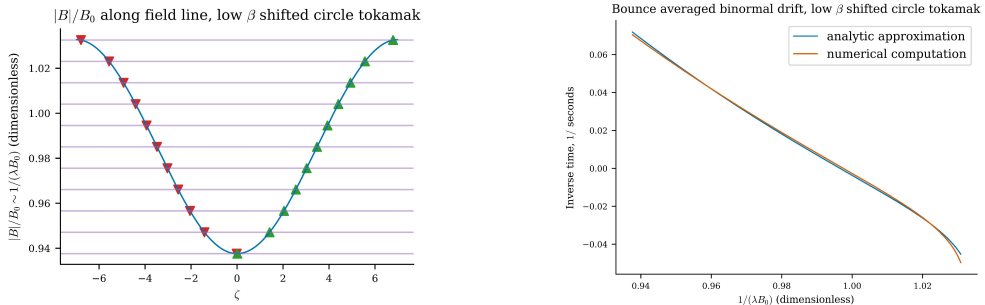
$$l_3 = \int_{-2\sin^{-1}(k)}^{2\sin^{-1}(k)} d\theta_P \sqrt{k^2 - \sin(\theta_P/2)^2} \theta_P \sin(\theta_P) = \frac{32}{9} [E + (k^2 - 1)^2 K] \quad (\text{B } 18)$$

$$l_4 = \int_{-2\sin^{-1}(k)}^{2\sin^{-1}(k)} \frac{d\theta_P}{\sqrt{k^2 - \sin(\theta_P/2)^2}} (\sin(\theta_P))^2 = \frac{16}{3} [(-1 + 2k^2)E - (-1 + k^2)K] \quad (\text{B } 19)$$

$$\begin{aligned} l_5 = & \int_{-2\sin^{-1}(k)}^{2\sin^{-1}(k)} d\theta_P \sqrt{k^2 - \sin(\theta_P/2)^2} (\sin(\theta_P))^2 \\ = & \frac{32}{30} [2(1 - k^2 + k^4)(E - (k^2 - 1)K) - (1 - 3k^2 + 2k^4)k^2 K] \quad (\text{B } 20) \end{aligned}$$

$$l_6 = \int_{-2\sin^{-1}(k)}^{2\sin^{-1}(k)} \frac{d\theta_P}{\sqrt{k^2 - \sin(\theta_P/2)^2}} \cos(\theta_P) = [8E - 4K] \quad (\text{B } 21)$$

$$l_7 = \int_{-2\sin^{-1}(k)}^{2\sin^{-1}(k)} d\theta_P \sqrt{k^2 - \sin(\theta_P/2)^2} \cos(\theta_P) = \frac{4}{3} [(2k^2 - 1)E - (k^2 - 1)K] \quad (\text{B } 22)$$



(a) For a given pitch marked by a horizontal line,  $|v_{\parallel}| = 0$  at the bounce points marked by triangles.

(b) Binormal drift.

Figure 8: In a shifted-circle model, we can approximately solve for analytic expressions for bounce averaged drifts and test the accuracy of the bounce averaging.

where  $K$  and  $E$  are complete elliptic integrals of the first and second kind, respectively. Using these formulae, to lowest order the analytical bounce-averaged drift is

$$\begin{aligned}
 \overline{v_D} &= \frac{1}{G_0} \left\{ \left( f_3 \frac{\alpha_{\text{MHD}}}{B_0^2} - f_2 \frac{\hat{s}}{2} \right) l_1 + \frac{f_2}{2} \left( \hat{s} l_3 - \frac{\alpha_{\text{MHD}}}{B_0^4} l_5 + l_7 \right) \right. \\
 &\quad \left. + \frac{f_2}{2} \left[ -\hat{s} (l_0 - l_2) - \frac{\alpha_{\text{MHD}}}{B_0^4} l_4 + l_6 \right] \right\} \\
 &= \frac{1}{G_0} \left( f_3 \frac{\alpha_{\text{MHD}}}{B_0^2} l_1 - \frac{f_2}{2} \left[ \hat{s} (l_0 + l_1 - l_2 - l_3) + \frac{\alpha_{\text{MHD}}}{B_0^4} (l_4 + l_5) - (l_6 + l_7) \right] \right) \quad (\text{B } 23)
 \end{aligned}$$

In figure 8b, the minor difference is a result of ignoring higher-order terms in the analytic approximation as the shifted circle model is only accurate up to  $\mathcal{O}(\varepsilon^2)$ .

## REFERENCES

- BOYD, J.P. 2013 *Chebyshev and Fourier Spectral Methods: Second Revised Edition*. Dover Publications.
- BOYD, JOHN P. & YU, FU 2011 Comparing seven spectral methods for interpolation and for solving the poisson equation in a disk: Zernike polynomials, logan–shepp ridge polynomials, chebyshev–fourier series, cylindrical robert functions, bessel–fourier expansions, square-to-disk conformal mapping and radial basis functions. *Journal of Computational Physics* **230** (4), 1408–1438.
- BRADBURY, JAMES, FROSTIG, ROY, HAWKINS, PETER, JOHNSON, MATTHEW JAMES, LEARY, CHRIS, MACLAURIN, DOUGAL, NECULA, GEORGE, PASZKE, ADAM, VANDERPLAS, JAKE, WANDERMAN-MILNE, SKYE & ZHANG, QIAO 2018 JAX: composable transformations of Python+NumPy programs.
- CONLIN, RORY, DUDT, DANIEL W, PANICI, DARIO & KOLEMEN, EGEMEN 2023 The DESC stellarator code suite. Part 2. Perturbation and continuation methods. *Journal of Plasma Physics* **89**, 955890305.
- D’HAESELEER, W. D., HITCHON, W. N. G., CALLEN, J. D. & SHOHEIT, J. L. 2012 *Flux coordinates and magnetic field structure: a guide to a fundamental tool of plasma theory*. Springer Science & Business Media.
- DREVLAK, M., BEIDLER, C. D., GEIGER, J., HELANDER, P. & TURKIN, Y. 2018 Optimisation of stellarator equilibria with rose. *Nuclear Fusion* **59**, 016010.
- DUDT, DANIEL, CONLIN, RORY, PANICI, DARIO, KOLEMEN, EGEMEN, UNALMIS, KAYA & KIM, PATRICK 2024 DESC.
- DUDT, DANIEL, CONLIN, RORY, PANICI, DARIO, KOLEMEN, EGEMEN, UNALMIS, KAYA & KIM, PATRICK 2025 DESC.
- DUDT, DW & KOLEMEN, E 2020 DESC: A stellarator equilibrium solver. *Physics of Plasmas* **27** (10).
- GAUR, RAHUL 2024 Omnigenous equilibria with enhanced stability: Dataset and analysis files. <https://doi.org/10.5281/zenodo.13887566>.
- GAUR, RAHUL, CONLIN, RORY, DICKINSON, DAVID, PARISI, JASON F, DUDT, DANIEL, PANICI, DARIO, KIM, PATRICK, UNALMIS, KAYA, DORLAND, WILLIAM D & KOLEMEN, EGEMEN 2024 Omnigenous stellarator equilibria with enhanced stability. *arXiv preprint arXiv:2410.04576* .
- HELANDER, PER 2014 Theory of plasma confinement in non-axisymmetric magnetic fields. *Reports on Progress in Physics* **77** (8), 087001.
- HELANDER, PER & SIGMAR, DIETER J 2005 *Collisional transport in magnetized plasmas*, , vol. 4. Cambridge university press.
- HIBBARD, GRETA, PANICI, DARIO, GAUR, RAHUL, UNALMIS, KAYA & KOLEMEN, EGEMEN 2024 Optimizing stellarators against energetic particle loss with desc. *Bulletin of the American Physical Society* .
- HIRSHMAN, S. P. & WHITSON, J. C. 1983 Steepest-descent moment method for three-dimensional magnetohydrodynamic equilibria. *The Physics of fluids* **26**, 3553.
- LANDREMAN, M., MEDASANI, B., WECHSUNG, F., GIULIANI, A., JORGE, R. & ZHU, C. 2021 SIMSOPT: A flexible framework for stellarator optimization. *Journal of Open Source Software* **6**, 3525.
- LAZERSON, SAMUEL, SCHMITT, JOHN, ZHU, CAO XIANG, BRESLAU, JOSHUA & STELLOPT DEVELOPERS, ALL 2020 Stellopt.
- MACKENBACH, RJJ, PROLL, JOSEFINE HE & HELANDER, P 2022 Available energy of trapped electrons and its relation to turbulent transport. *Physical Review Letters* **128**, 175001.
- NEMOV, VV, KASILOV, SV, KERNBICHLER, W & HEYN, MF 1999 Evaluation of  $1/\nu$  neoclassical transport in stellarators. *Physics of plasmas* **6** (12), 4622–4632.
- NEMOV, V. V., KASILOV, S. V., KERNBICHLER, W. & LEITOLD, G. O. 2008 Poloidal motion of trapped particle orbits in real-space coordinates. *Physics of Plasmas* **15** (5), 052501, arXiv: [https://pubs.aip.org/aip/pop/article-pdf/doi/10.1063/1.2912456/14080658/052501\\_1\\_online.pdf](https://pubs.aip.org/aip/pop/article-pdf/doi/10.1063/1.2912456/14080658/052501_1_online.pdf).
- NVIDIA CORPORATION 2020 Nvidia A100 tensor core gpu. <https://www.nvidia.com/en-us/data-center/a100/>, accessed: 26 February 2025.
- OLVER, F. W. J., OLDE DAALHUIS, A. B., LOZIER, D. W., SCHNEIDER, B. I., BOISVERT,

- R. F., CLARK, C. W., MILLER, B. R., B. V. SAUNDERS, H. S. COHL & M. A. McCLAIN, EDS. 2024 *NIST digital library of mathematical functions*. <https://dlmf.nist.gov/>, Release 1.2.2 of 2024-09-15.
- PANICI, DARIO, CONLIN, RORY, DUDT, DANIEL W, UNALMIS, KAYA & KOLEMEN, EGEMEN 2023 *The DESC stellarator code suite. Part 1. Quick and accurate equilibria computations*. *Journal of Plasma Physics* **89**, 955890303.
- SAPIENZA, FACUNDO, BOLIBAR, JORDI, SCHÄFER, FRANK, GROENKE, BRIAN, PAL, AVIK, BOUSSANGE, VICTOR, HEIMBACH, PATRICK, HOOKER, GILES, PÉREZ, FERNANDO, PERSSON, PER-OLOF & RACKAUCKAS, CHRISTOPHER 2024 *Differentiable programming for differential equations: A review*, arXiv: 2406.09699.
- SPITZER JR, LYMAN 1958 *The stellarator concept*. *The Physics of Fluids* **1**, 253–264.
- SPONG, D. A., HIRSHMAN, S. P., WHITSON, J. C., BATCHELOR, D. B., CARRERAS, B. A., LYNCH, V. E. & ROME, J. A. 1998 *J\* optimization of small aspect ratio stellarator/tokamak hybrid devices*. *Physics of Plasmas* **5** (5), 1752–1758.
- VELASCO, JL, CALVO, I, MULAS, S, SÁNCHEZ, E, PARRA, FI, CAPPÀ, A & OTHERS 2021 *A model for the fast evaluation of prompt losses of energetic ions in stellarators*. *Nuclear Fusion* **61**, 116059.